ChemPhysChem

Research Article
doi.org/10.1002/cphc.202200033

Chemistry
Europe
European Chemical
Societies Publishing

www.chemphyschem.org

Influence of Pt Alloying on the Fluorescence of Fully Inorganic, Colloidal Gold Nanoclusters

Anna R. Ziefuss,[a] Michael Willeke,[a] Matthias Miertz,[a] Alexander Heinemann,[a] Christoph Rehbock,[a] and Stephan Barcikowski*[a]

Noble metal alloy nanoclusters (NCs) are interesting systems as the properties of two or more elements can be combined in one particle, leading to interesting fluorescence phenomena. However, previous studies have been exclusively performed on ligand-capped NCs from wet chemical synthesis. This makes it difficult to differentiate to which extent the fluorescence is affected by ligand-induced effects or the elemental composition of the metal core. In this work, we used laser fragmentation in liquids (LFL) to fabricate colloidal gold-rich bi-metallic AuPt NCs in the absence of organic ligands and demonstrate the suitability of this technique to produce molar fraction series of 1nm alloy NC. We found that photoluminescence of ligand-free NCs is not a phenomenon limited to Au. However, even minute amounts of Pt atoms in the AuPt NCs lead to quenching and red-shift of the fluorescence, which may be attributed to the altered surface charge density.

Introduction

Monometallic metal nanoclusters (NC) have attracted strong interest in a variety of scientific research fields due to their characteristic quantum confinement, which leads to discrete structure,[1] size,[2] and surface coverage[3] dependent electronic transitions. This results in extraordinary physicochemical and molecular-like properties, directly affecting the discrete photoluminescence phenomena observed in these materials.[3–5] Scientists have successfully modified electronic transitions and related optical properties of NC by combining two or more metal species to form alloy NCs (e.g., AuAg,[6,7] AuCu,[8] AuPt[9,10]). Next to a combination of different material properties, bi-metallic NC can induce synergistic effects, resulting in enhanced catalytic activity or significantly shifted fluorescence signals.[11] Andolinia et al.[12] found that even small amounts of Cu in AuCu NCs can lead to a dramatic red-shift of the emission wavelength and an increased emission intensity. In contrast, Negishi et al.[7] observed a blue shift after doping Au NCs with Ag. Kothalawala et al.[13] incorporated up to 3 Pd atoms into the $Au_{144}(SR)_{60}$ icosahedral NC structure and found a decreased absorbance in the visible spectrum attributed to the inclusion of Pd atoms into the metal core rather than the staple motifs. Alloying Au

NCs with Pt was reported to increase the catalytic activity without affecting the fluorescence behaviour.[10] Contrary, Feng et al.[14] detected a decrease in emission and absorbance by successfully alloying glutathione-stabilized Au NCs with Pt, accompanied by increased peroxidase-like activity. Due to many existing monometallic NC systems with strongly deviating crystal structures, number of atoms, and surface ligand types, it is difficult to systematically predict the influence of heteroatoms on their intrinsic properties. However, some influencing factors could already be determined. The influence of heteroatoms on fluorescence is currently explained by a changed electropositivity of the metal core,[15] deviating crystal structures,[16] different numbers of valence electrons,[17] or charge effects on the surface.[18] The latter, however, is often not caused by the metal alone; covalently bound organic ligands are also known to cause ligand-metal-charge-transfer (LMCT) effects with the metal surface.[19] Such ligands are necessarily present during typical wet chemical synthesis based on the reduction of a metal precursor[5] and tend to dominate the features of the NCs. For example, $Au_{25}(HSG)_{18}$ (with HSG = glutathione) contains only 3.75% of gold atoms.[20] This makes it difficult to clearly assign the above effects to either LMCT or metal-metal charge-transfer (MMCT) effects.

Recently, Ziefuss et al.[21] have successfully prepared monometallic, completely inorganic NC using a laser-based approach without organic ligands. They first irradiated a solid Au target using the laser ablation in liquids (LAL) method to obtain a well-dispersed nanoparticle (NP) colloid. The colloid was then re-irradiated using laser fragmentation in liquids (LFL), and protoplasmonic Au NCs smaller than 3 nm were obtained after centrifugation. A detailed description of the LAL[22] and the followed LFL[23,24] process can be found elsewhere. Here, LFL leads to particles with a mean diameter of 2.9 nm[23] without an observable fluorescence behaviour. However, a mechanical ultracentrifugation step enables a proper size separation.[21] Larger and core-dominated NCs (> 1 nm) showed size-dependent specific emission around 350–400 nm, while smaller, sur-

[a] Dr. A. R. Ziefuss, M. Willeke, M. Miertz, Dr. A. Heinemann, Dr. C. Rehbock, Prof. Dr. S. Barcikowski
Technical Chemistry I and Center for Nanointegration Duisburg–Essen (CENIDE),
University Duisburg–Essen
Universitätsstraße 7, 45141 Essen (Germany)
E-mail: stephan.barcikowski@uni-due.de

face-dominated nanoclusters (< 1 nm) exhibited an additional energy-rich emission state at around 300 nm. In both cases, the emission intensity has been a function of the surface charge density.[21] Thereby, the core emission of the larger-sized fraction increases with an increasing number of surface charges. The smaller-sized fraction does not show this behaviour. Here, no differences in the core emission could be observed. We found the HOMO is dominated by contributions from the surface located deprotonated oxygen (which is responsible for the increased surface charge density). The lower observed surface-emission intensity can be explained by an overlap of this HOMO with the LUMO, which is primarily located at the particle's core.[21] However, the influence of heteroatoms on the LFL synthesis and on the photoluminescence properties of fully inorganic NCs has not been determined to date.

Hence, we generated ligand-free monometallic Au NCs, Pt NCs, and gold-rich bimetallic AuPt NCs with composition of $Au_{98}Pt_2$ and $Au_{90}Pt_{10}$. We compared the optical behaviour with that of their monometallic equivalents and an *ex-situ* mixture of monometallic Au and Pt NC with the same global elemental composition as the alloy.

Results and Discussion

The production of AuPt alloy NC is a three-step procedure, starting with LAL of a sintered metallic target produced by mixing Au and Pt micro powders in a defined ratio (see method part) as previously described in the literature.[25] The process leads to colloidal nanoparticles (NP) with a broad hydrodynamic size distribution. Hence, these nanoparticles require further downsizing steps to reach the NCs size range. However, LFL requires particles larger than the fragmentation threshold diameter (for Au, d > 13.4 nm[23]), so that separation of smaller particle fractions was necessary before LFL. Here, we used centrifugation as described in Ref. [23]. The resulting particle size distributions with mean diameter 50–60 nm can be found in Figure S2A. We have determined the actual composition of the produced NPs for the 90:10 (Au:Pt) composition by TEM-EDX single particle analysis (see EDX summed up line spectrum in Figure 1). Note that the EDX-mapping pixel intensity is not linearly correlated with the composition, a pixel is displayed where the elemental threshold count rate is exceeded, showing homogeneous elemental distribution in the particle volume but no direct quantitative information. Such solid-solution structure has been reported earlier for laser-generated AuPt particles.[25–27]

In addition, we prepared a 98:2 (Au:Pt) atomic mixture target and EDX-analysis of this target verified the 98:2 atomic ratio (Figure 1B). The Pt content in the nanoparticles fabricated from these targets was too low to be verifiably measured via EDX. However, following Ref. [25,28–30] the composition of the nanoparticles after laser processing equals the mixing ratio of the micro powder for target preparation and can thereby be easily tuned by the mixing ratio[31] For example, Neumeister et al.[29] verified this for $Ag_{100-x}Au_x$-alloys (x = 10 to 90% in 10% intervals), and Waag et al.[28] expanded this knowledge to even
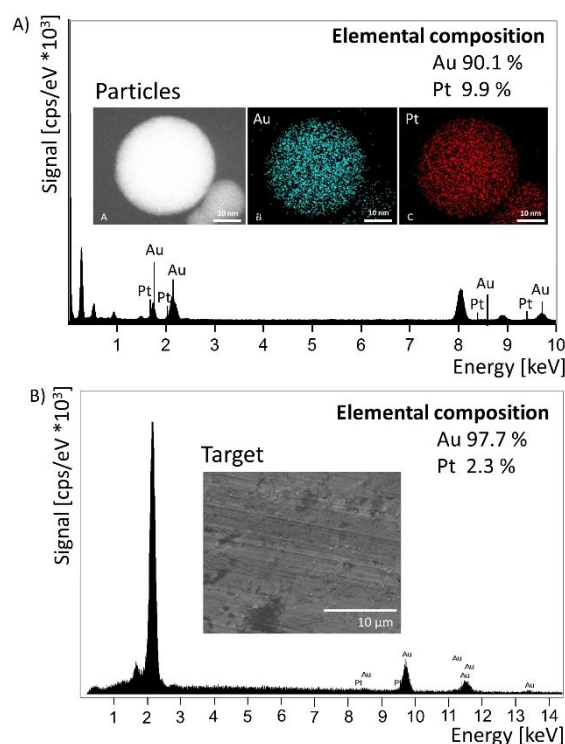

Figure 1. A) EDX results of $Au_{90}Pt_{10}$ NPs after LAL incl. TEM-EDX mapping of this particle to show the homogeneity of the elemental composition. B) EDX results of the $Au_{98}Pt_2$ sintered powder target.

quinary alloys, at the example of high entropy CoCrFeMnNi-alloy systems. Furthermore, the pronounced differences in the absorbance spectra of the Au, Pt, $Au_{98}Pt_2$, and $Au_{90}Pt_{10}$ colloids (Figure S3) suggest a difference in composition. Note that the differences in the absorbance spectra[32] (Figure S3) will also affect the LFL process, especially its efficiency since the energy input critically depends on the absorption at the LFL wavelength (intensity and absorption cross-section). To overcome these limitations, we have performed the LFL in a free-liquid jet with single pulse per volume element (PPV)[23] conditions and cycled the colloid as long as we could detect changes in the absorbance spectra (Figure S3). The resulting mean diameter determined by analytical disk centrifugation (ADC) varied from 2.7 nm (Au NPs) to 3.1 nm (Pt NPs) (see also Figure S4); however, ultracentrifugation steps enable access to monodisperse NC with a similar size distribution for all produced NCs (see Figure 2). Please note that we used analytical ultracentrifugation (AUC) to determine the resulting hydrodynamic particle size distribution of the NCs, which is a powerful tool with a resolution in the Angström range.[21,33] Here, the particle size determination is based on a measurement of the sedimentation behaviour of the particles, which can be influenced by the particles' density, diffusion, and surface charge in addition to the particle size. While charge effects (as a directed counter-force to sedimentation) can reduce the sedimentation velocity, diffusion should lead to a broadening of the sedimentation velocity distribution. Since different materials are compared with each other here, these influencing factors can become
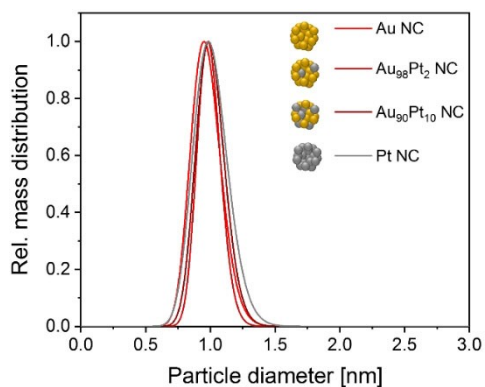
ChemPhysChem

Research Article
doi.org/10.1002/cphc.202200033

**Chemistry
Europe**
European Chemical
Societies Publishing

Figure 2. Normalized mass-weighted particle size distribution of inorganic Au NCs, Pt NCs, and AuPt NCs with different Pt molar fractions produced with laser fragmentation in the absence of organic ligands.

quite relevant and lead to slight deviations in the distribution. Therefore, we will not discuss the minor differences in detail

and assume comparable particle sizes for the NC, in particular as the density of Au and Pt is almost the same.

Although all analysed samples possess a comparable mean diameters (1 nm) and size distribution widths (Figure 2), we found a distinguishable optical behavior (Figure 3A, B). The Au NCs show an absorbance peak at 277 nm, which cannot be observed for Pt NC. The gold-rich bi-metallic AuPt NCs also show this absorbance peak; however, a slight decrease with increasing Pt content can be observed (Figure 3A). This is in good agreement with the study of Kothalawala et al.[13] as they found that alloying of $Au_{144}(SR)_{60}$ with Pd leads to a diminution of the Au NCs absorbance features.

Besides, we found a change in the fluorescence emission with increasing Pt content in the NCs. The emission behaviour of ligand-free Au NCs has been discussed previously.[21] A size-tuneable core emission between 350 nm and 400 nm and a surface-related emission at 300 nm were detected for Au NCs smaller than 1 nm, originating from changed crystal structures or quantization of energy states.[21] The emission at around 300 nm decreases in the case of $Au_{98}Pt_2$ and $Au_{90}Pt_{10}$ NCs (Figure 3B), which could be due to a lower absorption efficiency
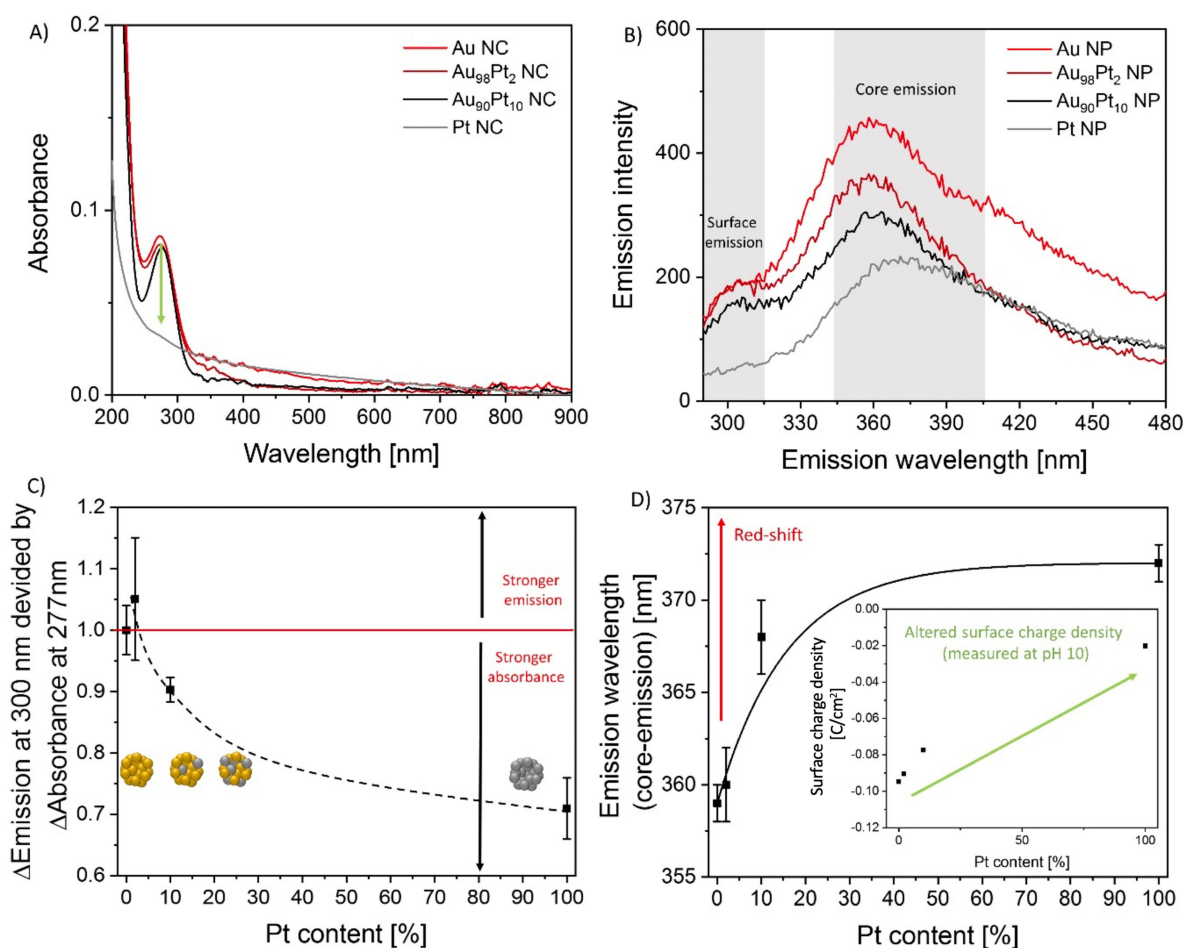

Figure 3. Characterisation of optical properties of Au and Pt NCs and two Au-rich AuPt-alloy NCs at a concentration of 0.5 mg/L. A) absorbance spectra, B) emission spectra after excitation at 250 nm. (Emission plotted excluding the excitation wavelength range). C) Relative change of normalized emission intensity divided by a decrease of normalized absorbance using Au NCs as a reference. D) An increasing Pt content leads to a red shift of the emission between 355 and 375 nm. Error bars correspond to the standard deviation after measurement of three samples each.

ChemPhysChem

Research Article
doi.org/10.1002/cphc.202200033

**Chemistry
Europe**
European Chemical
Societies Publishing

(Figure 3A). These findings, showing a reduction of absorbance and emission intensity with increasing Pt content triggered the question of whether these phenomena are directly proportional, and the reduced absorbance is the only cause for lower emission intensities. To tackle this question, we calculated the quotient between the emission intensity at 300 nm (ΔEmission) and the absorbance at 277 nm (ΔAbsorbance) and normalized it by the corresponding quotient for pure AuNC. Consequently, a quotient >1 corresponds to an intensified emission intensity, while a quotient <1 would indicate an emission intensity quenching. For the sample with 2% Pt content, a value close to 1 is found. However, the addition of 10% Pt to the AuNC leads to a drastic reduction of this value, which gets more pronounced for pure Pt. From these findings we can conclude: I) The strong reduction in emission intensity following the alloying of AuNC with Pt is not only caused by the reduced absorbance. II) Non-radiative decay channels for the absorbed light get more pronounced with increasing Pt content, a phenomenon which could be related to surface defects or different electron densities due to the laser-fabricated alloy NCs (hypotheses discussed below in more detail). In this context, it should be noted that these phenomena were only found for the surface-attributed emission peaks at 300 nm. Hence the presented ratio does not correspond to the total quantum yield as it is usually calculated by integrating the entire absorbance and emission spectra. Similarly, the core emission intensity at ~350 nm decreases significantly and shows an exponential red shift with increasing Pt content (Figure 3D). Please note that we could not determine the exact composition of the alloy NCs as the particle size was too small to get an appropriate signal during EDX measurements. However, to exclude a separation of the pure elements and the formation of individual monometallic PtNC and AuNC, we compared the absorbance of the alloy particles after LFL with a mixture of the corresponding monometallic NC at the same elemental ratio and found a clearly distinguishable optical behaviour. While the $Au_{90}Pt_{10}$ particles prepared by LFL from $Au_{90}Pt_{10}$ alloy target still show an absorbance peak at 277 nm, the mixture of the pure elements in the same ratio lacks this feature. Furthermore, time-resolved measurements of the individual single element particle mixtures show no changes over time. Hence, we can exclude atom exchange reactions between single metallic alloy NCs in solution as a competing particle formation mechanism (Figure S5).

These observations are highly interesting, and we must consider the following two factors, which can influence the intensity and position of the core or surface emission in alloyed NCs. Note that we can exclude a particle size effect as all particles show comparable size distributions (Figure 2).

(i) Au and Pt are known to crystalize in an fcc crystal structure. We may assume a solid solution structure in the NC as Pt is well soluble in Au at these low Pt contents as already verified for the educt nanoparticles (Figure 1). However, the unit cells show a different physical dimension caused by different lattice constants (Au: 408.0 pm, Pt: 392.4 pm)[34] and different atomic radii (Au: 144 pm, Pt: 138.5 pm).[35] Hence, we can assume that the unit cell shrinks due to the incorporation

of Pt into the Au fcc. On the other hand, it is known that lattice constant dilatation of some percent happens for very small NPs.[36] The introduction of small amounts of Pt in Au-based NC is further expected to stabilize defects in the crystal structure, mainly referable to the different atomic radii.[34,35] Even small amounts of Pt < 10% in the NC lead to a red-shifted core emission, non-linearly correlated with the Pt content. Hence, we could speculate on a potential correlation between an increasing defect density and a change of the optical properties. The defects of AuPt NCs may originate from or could be further intensified by the LFL synthesis process. Re-irradiation of larger NPs initiates a phase explosion,[24,37] followed by sudden cooling of the fragmentation plume,[24] causing the spontaneous solidification in the thermodynamically unfavoured distorted (3|1|1) surface lattice structure.[21]

It has been reported that laser-generated NPs are often defect-rich, caused by cooling rate of 10^{12}–10^{13} K/s during this kinetically-controlled synthesis.[31] Recently, Zhigilei et al. reported that NCs are ejected directly into the dense cold water during LFL,[37] indicating even faster cooling-rates. The distortion depends on the cooling rate, atomic radius, and material-dependent properties. Since the surface-emission vanishes completely in Pt NCs, it can be presumed that the Pt NCs solidify differently compared to Au NCs during LFL. Unfortunately, it has not been possible to determine the crystal structure of the particles (e.g. by XRD or XAS) as the concentration of the particles is too low. However, in our previous work on Au NCs,[24] we performed in-situ X-ray absorption spectroscopy to determine the structure of the particle's core and found clear evidence of an fcc.

(ii) Moreover, different energy states and (Highest Occupied Molecular Orbital) HOMO – (Lowest Unoccupied Molecular Orbital) LUMO gaps could result in different electronic states. In this context, particularly the fact that Pt atoms possess less valence electrons than Au atoms should be relevant and would result in an alloy NC with a pronounced electron deficiency, which would go along with a reduced surface charge density. According to Ohshima et al.[38] the surface charge density can be correlated to the zeta potential. Hence, we performed zeta potential measurements of our AuPt NC and found a decreasing zeta potential (surface charge density) with increasing Pt content (inset Figure 2D), which confirms our hypothesis even though the zeta potential was measured using dynamic light scattering at 633 nm, and the signal was noisy as the colloid's absorbance at this wavelength is very low. These findings are in accordance with our previous work on Au NCs,[21] where reduced surface charge density went along with a quenched fluorescence emission intensity, a trend similar to the one reported here for AuPt alloy NC.

Conclusions

In summary, we succeeded in producing fully inorganic bimetallic AuPt and monometallic Pt NCs and compared their properties with fully inorganic Au NCs. Minute amounts of Pt doping to create PtAu NCs lead to a (i) quenched energy-rich

surface emission, (ii) a red-shifted and quenched core emission, and (iii) a drastic decrease of the surface charge density. Point (i) and (iii) are possibly correlated and indicate the surface charge density-dependent emission that was already found in Ref. [13]. Point (ii), the red-shifted emission with increasing Pt content could be due to distortions in the crystal structure and the formation of defects, a hypothesis to be further examined in follow-up experiments. Here, suitable concentration techniques are to be developed to allow crystal structure evaluations e.g., by XAS. These studies further highlight the suitability of the LFL technique to produce alloy NCs with controlled composition and free of organic surface adsorbates. This trend should be explored in producing AuPt alloy series over a broader range of compositions as well as the transfer to other alloy NCs like AgAu or CuAu to further understand correlations between core composition and photoluminescence of fully inorganic NCs.

Experimental Section

The laser-based production of fully inorganic NC is a three-step procedure containing laser ablation in liquids (LAL), laser fragmentation in liquids (LFL), and a subsequent ultrafiltration step. All steps, including the characterization of intermediate products, will be explained in the following.

Pulsed LAL

A ps-pulsed laser (Ekspla, Atlantics series, 10 ps, 1064 nm, 8.8 mJ, 100 kHz) is focused on a bulk target (Au in case of Au NCs and Pt in case of Pt NCs) or a sintered powder target in case of bi-metallic NC, which was in each case located in a 30 mL batch chamber filled with ultra-pure water. The sintered powder targets contained micro powders in an atomic ratio of 98% Au and 2% Pt in the case of $Au_{98}Pt_2$ NC and 90% Au and 10% Pt in the case of $Au_{90}Pt_{10}$ NC. The sintering was carried out at 800 °C (which is 80% of the melting point so that the highest yield of alloy particles with the narrowest composition range can be expected[39]) for 24 h. It was required to densify the target surface to prevent fragments from detaching during the LAL process and to ensure that particles with an even elemental distribution ruled by the target composition are obtained. We produced colloids with broad size distributions and centrifuged the as produced colloidal solutions (Hettich, 67.1 g-force, 70 min) to separate particles smaller than 20 nm because we know – at least for Au – that the absorption cross-section of those particles is too small to absorb enough energy for a successively required LFL process.[23] The size distribution of as produced particles can be found in Figure S1. Even small amounts of Pt dramatically affect the colour of the colloidal solutions (Figure S1 B–D). We observed a drastic decrease in the Au NP surface plasmon resonance intensity even for the sample with 2% Pt (Figure 1C). This indeed influences the amount of absorbed light, which will, following Ref. [23], affect the LFL efficiency in the successive LFL.

Pulsed LFL

The LFL was performed in a free-liquid jet as already described in Ref. [21,23]. In short, we re-irradiated the colloids depicted in Figure 1A with a ns-pulsed laser (Innolas, 9, ns, 100 Hz, 84 mJ, 1.6 J/m²) at 532 nm. The laser spot diameter and the jet dimensions were adjusted so that each volume element of the liquid jet was hit at least once by the laser (PPV; pulses per volume element). However, because of the gaussian laser profile and the attenuation of the laser beam in the axial direction, some particles stay unirradiated, so we needed multiple cycles to reach fragmentation of each educt NP (Figure S2). As soon as no change in absorption could be detected, the fragmentation was stopped, and we measured the particle size (Figure S3 D) using the analytical disc centrifuge (ADC, CPS Instruments DC 24000, 24000 rpm). In Ref. [23,40], we have determined a lower measurement limit of 2 nm, so this method is a first approximation to identify particle fractions > 3 nm, which must be removed by ultrafiltration. The fragmentation was done using a colloidal solution at a mass concentration of 7.5 mg/L. Measurements of the particle composition were not possible yet, as typical characterization methods require much higher concentrations. However, while working with bimetallic particles, the mass composition of the elements is an important factor. The scale-up of particle production and increasing the concentration through supporting the product particles on microparticles or embedding them in gels is necessary for follow-up studies. However, that the bimetallic character is preserved is already indicated recognized by the colloid's color after LFL. Au NCs are orange (Figure 1A), whereas the bimetallic equivalents show a rather greyish shade (Figure 1B–C). An aggregation of particles could also explain a greyish color but, we can observe this neither in the UV-Vis nor in ADC measurements.

The colloidal solution after LFL contained particles that are larger than typical nanocluster sizes. We performed ultra-filtration using centrifugal filters (Merk-millipore) to remove this size fraction with a molecular weight cut-off of 50 kDa. The centrifugation was done in a Hettich centrifuge at 4000 rpm (15 min). The filtrate was removed and used as a educt for a second centrifugal step using filters with a MWCO of 3 kDa. The filtrate contains the final product in a very low concentration. To concentrate these particles, we used a rotary evaporator (7 mbar, 45 °C). We determined the particle mass concentration with an inductively coupled plasma with mass spectrometric detection (ICP-MS, Perkin Elmer Sciex – ELAN 6000).

Nanocluster Characterization

The particle sizes were analyzed using an analytical ultracentrifuge (AUC) (Beckman-Coulter). We measured the sedimentation profile with an absorbance optic at 280 nm (12 h, 20 °C) and evaluated the sedimentation behaviour with the license-free software "Sedfit". The absorbance spectra were measured in the range of 190 nm–900 nm using a tabletop device from Thermo Scientific (Evolution 201). The emission behaviour was measured in the range of 200–800 nm after excitation at 250 nm (Variant Eclipse). Zeta-potential measurements were done with the Nano ZS (Malvern). Here, the surface charge density was calculated following Ref. [38].

Acknowledgements

Conflict of Interest

The authors declare no conflict of interest.

Data Availability Statement

The data that support the findings of this study are available from the corresponding author upon reasonable request.

[1] L. Zhang, E. Wang, *Nano Today* **2014**, *9*, 132–157.

[2] J. Zheng, C. Zhang, R. M. Dickson, *Phys. Rev. Lett.* **2004**, *93*, 77402.

[3] Z. Wu, R. Jin, *Nano Lett.* **2010**, *10*, 2568–2573.

[4] R. Jin, C. Zeng, M. Zhou, Y. Chen, *Chem. Rev.* **2016**, *116*, 10346–10413.

[5] I. Chakraborty, T. Pradeep, *Chem. Rev.* **2017**, *117*, 8208–8271.

[6] a) R. D. Corpuz, Y. Ishida, M. T. Nguyen, T. Yonezawa, *Langmuir* **2017**, *33*, 9144–9150; b) K. Loza, M. Heggen, M. Epple, *Adv. Funct. Mater.* **2020**, *30*, 1909260.

[7] X. Dou, X. Yuan, Y. Yu, Z. Luo, Q. Yao, D. T. Leong, J. Xie, *Nanoscale* **2014**, *6*, 157–161.

[8] a) G. Barcaro, A. Fortunelli, G. Rossi, F. Nita, R. Ferrando, *J. Phys. Chem. B* **2006**, *110*, 23197–23203; b) P.-C. Chen, J.-Y. Ma, L.-Y. Chen, G.-L. Lin, C.-C. Shih, T.-Y. Lin, H.-T. Chang, *Nanoscale* **2014**, *6*, 3503–3507.

[9] N. Xu, L. Meng, H.-W. Li, D.-Y. Lu, Y. Wu, *Mikrochim. Acta* **2018**, *185*, 294.

[10] Y. Chen, X.-Y. Ge, S.-Y. Cen, A.-J. Wang, X. Luo, J.-J. Feng, *Sens. Actuators B* **2020**, *311*, 127931.

[11] X. Yuan, X. Dou, K. Zheng, J. Xie, *Part. Part. Syst. Charact.* **2015**, *32*, 613–629.

[12] C. M. Andolina, A. C. Dewar, A. M. Smith, L. E. Marbella, M. J. Hartmann, J. E. Millstone, *J. Am. Chem. Soc.* **2013**, *135*, 5266–5269.

[13] N. Kothalawala, C. Kumara, R. Ferrando, A. Dass, *Chem. Commun.* **2013**, *49*, 10850–10852.

[14] J. Feng, P. Huang, F.-Y. Wu, *Analyst* **2017**, *142*, 4106–4115.

[15] X. Kang, M. Zhu, *Chem. Soc. Rev.* **2019**, *48*, 2422–2457.

[16] Z. Gan, J. Chen, L. Liao, H. Zhang, Z. Wu, *J. Phys. Chem. Lett.* **2018**, *9*, 204–208.

[17] X. Kang, Y. Li, M. Zhu, R. Jin, *Chem. Soc. Rev.* **2020**, *49*, 6443–6514.

[18] R. Kazan, U. Müller, T. Bürgi, *Nanoscale* **2019**, *11*, 2938–2945.

[19] a) R. R. Nasaruddin, T. Chen, N. Yan, J. Xie, *Coord. Chem. Rev.* **2018**, *368*, 60–79; b) M. B. Newmai, P. S. Kumar, *AIP Conf. Proc.* **2016**, *1728*, 1, 050111.

[20] M. Zhou, Y. Song, *J. Phys. Chem. Lett.* **2021**, *12*, 1514–1519.

[21] A. R. Ziefuss, T. Steenbock, D. Benner, A. Plech, J. Göttlicher, M. Teubner, B. Grimm-Lebsanft, C. Rehbock, C. Comby-Zerbino, R. Antoine, et al., *Adv. Mater.* **2021**, *33*, e2101549.

[22] S. Scaramuzza, M. Zerbetto, V. Amendola, *J. Phys. Chem. C* **2016**, *120*, 9453–9463.

[23] A. R. Ziefuß, S. Reichenberger, C. Rehbock, I. Chakraborty, M. Gharib, W. J. Parak, S. Barcikowski, *J. Phys. Chem. C* **2018**, *122*, 22125–22136.

[24] A. R. Ziefuss, S. Reich, S. Reichenberger, M. Levantino, A. Plech, *Phys. Chem. Chem. Phys.* **2020**, *22*, 4993–5001.

[25] J. Zhang, D. N. Oko, S. Garbarino, R. Imbeault, M. Chaker, A. C. Tavares, D. Guay, D. Ma, *J. Phys. Chem. C* **2012**, *116*, 13413–13420.

[26] F. Waag, R. Streubel, B. Gökce, S. Barcikowski, *Appl. Nanosci.* **2021**, *11*, 1303–1312.

[27] a) D. N. Oko, S. Garbarino, J. Zhang, Z. Xu, M. Chaker, D. Ma, D. Guay, A. C. Tavares, *Electrochim. Acta* **2015**, *159*, 174–183; b) D. N. Oko, J. Zhang, S. Garbarino, M. Chaker, D. Ma, A. C. Tavares, D. Guay, *J. Power Sources* **2014**, *248*, 273–282.

[28] F. Waag, Y. Li, A. R. Ziefuß, E. Bertin, M. Kamp, V. Duppel, G. Marzun, L. Kienle, S. Barcikowski, B. Gökce, *RSC Adv.* **2019**, *9*, 18547–18558.

[29] A. Neumeister, J. Jakobi, C. Rehbock, J. Moysig, S. Barcikowski, *Phys. Chem. Chem. Phys.* **2014**, *16*, 23671–23678.

[30] D. Tiedemann, U. Taylor, C. Rehbock, J. Jakobi, S. Klein, W. A. Kues, S. Barcikowski, D. Rath, *Analyst* **2014**, *139*, 931–942.

[31] S. Reichenberger, G. Marzun, M. Muhler, S. Barcikowski, *ChemCatChem* **2019**, *11*, 4489–4518.

[32] a) S. Moniri, M. Reza Hantehzadeh, M. Ghoranneviss, M. Asadi Asadabad, *Eur. Phys. J. Plus* **2017**, *132*, 13413; b) A. Joplin, S. A. Hosseini Jebeli, E. Sung, N. Diemler, P. J. Straney, M. Yorulmaz, W.-S. Chang, J. E. Millstone, S. Link, *ACS Nano* **2017**, *11*, 12346–12357.

[33] K. L. Planken, H. Cölfen, *Nanoscale* **2010**, *2*, 1849–1869.

[34] S. M. Foiles, M. I. Baskes, M. S. Daw, *Phys. Rev. B: Condens. Matter Mater. Phys.* **1986**, *33*, 7983–7991.

[35] L.-Q. Chen, Y. Gu, *Physical Metallurgy* **2014**, 2807–2835.

[36] C. Solliard, M. Flueli, *Surf. Sci.* **1985**, *156*, 487–494.

[37] H. Huang, L. V. Zhigilei, *J. Phys. Chem. C* **2021**, *125*, 13413–13432.

[38] K. Makino, H. Ohshima, *Langmuir* **2010**, *26*, 18016–18019.

[39] F. Waag, W. I. M. A. Fares, Y. Li, C. Andronescu, B. Gökce, S. Barcikowski, *J. Mater. Sci.* **2022**, *57*, 3041–3056.

[40] A. R. Ziefuß, S. Barcikowski, C. Rehbock, *Langmuir* **2019**, *35*, 6630–6639.